FULL PAPER

# Magnetically Decorated Multiwalled Carbon Nanotubes as Dual MRI and SPECT Contrast Agents

*Julie Tzu-Wen Wang, Laura Cabana, Maxime Bourgognon, Houmam Kafa, Andrea Protti, Kerrie Venner, Ajay M. Shah, Jane K. Sosabowski, Stephen J. Mather, Anna Roig, Xiaoxing Ke, Gustaaf Van Tendeloo, Rafael T. M. de Rosales, Gerard Tobias,* and Khuloud T. Al-Jamal**

**Carbon nanotubes (CNTs) are one of the most promising nanomaterials to be used in biomedicine for drug/gene delivery as well as biomedical imaging. This study develops radio-labeled, iron oxide-decorated multiwalled CNTs (MWNTs) as dual magnetic resonance (MR) and single photon emission computed tomography (SPECT) contrast agents. Hybrids containing different amounts of iron oxide are synthesized by in situ generation. Physicochemical characterisations reveal the presence of superparamagnetic iron oxide nanoparticles (SPION) granted the magnetic properties of the hybrids. Further comprehensive examinations including high resolution transmission electron microscopy (HRTEM), fast Fourier transform simulations, X-ray diffraction, and X-ray photoelectron spectroscopy assure the conformation of prepared SPION as $\gamma$-$Fe_2O_3$. High $r_2$ relaxivities are obtained in both phantom and in vivo MRI compared to the clinically approved SPION Endorem. The hybrids are successfully radio labeled with technetium-99m through a functionalized bisphosphonate and enable SPECT/CT imaging and $\gamma$-scintigraphy to quantitatively analyze the biodistribution in mice. No abnormality is found by histological examination and the presence of SPION and MWNT are identified by Perls stain and Neutral Red stain, respectively. TEM images of liver and spleen tissues show the co-localization of SPION and MWNTs within the same intracellular vesicles, indicating the in vivo stability of the hybrids after intravenous injection. The results demonstrate the capability of the present SPION–MWNT hybrids as dual MRI and SPECT contrast agents for in vivo use.**

## 1. Introduction

Nanomaterials constitute a new class of imaging agents in biomedical imaging. Because of the possession of large surface area per unit and the capability of further engineering, they often serve as a platform to facilitate imaging via the incorporation, either covalently or non-covalently, of various imaging probes such as fluorophores, radiotracers or magnetic resonance (MR) imaging contrast agents.[1–4] Carbon nanotubes (CNTs) are considered one of the most promising nanomaterials to be used for biomedicine applications as delivery vectors for drugs or genes.[5–7] CNTs have also been employed for in vivo imaging either through conventional linking to the above mentioned imaging molecules or can be captured directly using Raman spectroscopy,[8] NIR fluorescence microscopy,[9] photoacoustic imaging[10] or ultrasonography[11] all relying on their inherent physical properties. However, satisfactory sensitivity and spatial resolution remain the major challenges.

Although optical imaging is still the leading imaging modality in

Dr. J. T.-W. Wang, M. Bourgognon, H. Kafa, Dr. K. T. Al-Jamal
Institute of Pharmaceutical Science
King's College London
London, SE1 9NH, UK
E-mail: gerard.tobias@icmab.es
L. Cabana, Dr. A. Roig, Dr. G. Tobias
Institut de Ciència de Materials de Barcelona (ICMAB-CSIC)
Campus UAB, 08193, Bellaterra, Barcelona, Spain
E-mail: khuloud.al-jamal@kcl.ac.uk
Dr. A. Protti, Dr. R. T. M. de Rosales
Division of Imaging Sciences and Biomedical Engineering
King's College London
St. Thomas' Hospital, London, SE1 7EH, UK
Dr. A. Protti, Prof. A. M. Shah
Cardiovascular Division, James Black Centre
King's College London British Heart Foundation Centre of Excellence
London, SE5 9NU, UK
K. Venner
UCL Institute of Neurology
University College London
London, WC1N 3BG, UK
Dr. J. K. Sosabowski, Prof. S. J. Mather
Centre for Molecular Oncology
Barts Cancer Institute,
Queen Mary University of London
London, EC1A 7BE, UK
Dr. X. Ke, Prof. G. Van Tendeloo
Electron Microscopy for Materials Research (EMAT)
University of Antwerp
Groenenborgerlaan 171, B-2020, Antwerp, Belgium

DOI: 10.1002/adfm.201302892

laboratory-based biomedical research mainly due to its convenience and low cost,[12] magnetic resonance imaging and nuclear imaging are currently the mainstream clinical diagnostic approaches. MRI is already a standard medical imaging technique which offers excellent spatial and temporal resolution, and good soft tissue contrast.[13] Nuclear imaging including single photon emission computed tomography (SPECT) and positron emission tomography (PET) involves the use of radioisotopes and has the advantages over other modalities of high sensitivity and the possibility to perform functional imaging.[14] The concept to establish multimodality imaging techniques is not new since each imaging modality has its own strength and weaknesses. From material scientists' points of view, efforts have been made in the development of multimodal imaging contrast agents.[15] Here we propose magnetically decorated multi-walled CNTs (MWNTs) as dual MRI and SPECT contrast agents.

Many studies have been conducted to employ CNTs for MRI by incorporating paramagnetic gadolinium ($Gd^{3+}$) or superparamagnetic iron oxide nanoparticles (SPION) into CNTs.[16–22] The two contrast agents are both clinically approved although showing opposite effect on a MR image. $Gd^{3+}$ serves mainly as a positive contrast agent which increases proton spin-lattice relaxation rates ($R_1$); iron oxide instead is a negative contrast agent by increasing spin-spin proton transverse relaxation rates $R_2$ and $R_2$*. Although $Gd^{3+}$-based contrast agents (GBC) are generally considered safe after chemical conjugation with organic chelating ligands, concern remains in their in vivo stability as free gadolinium ions are toxic.[23] There are also reports of adverse effects on using GBC in patients with impaired renal function.[24] In this regard, iron oxide nanoparticles which exhibit superparamagnetic properties have been used as negative MRI contrast agents in the clinic since they are biodegradable and can be incorporated into normal iron metabolism in the body.[25,26] A $Gd^{3+}$-conjugated ultra-short single-walled CNT (SWNT) nanocomposite was reported as a CNT-based MRI contrast agent for the first time in 2005.[16] Together with a subsequent study,[17] this type of $Gd^{3+}$-SWNTs induced low toxicity in vitro and reported both high $R_1$ and $R_2$ relaxation properties. The first approach to employ CNT/iron oxide for MR imaging was described by Choi et al. who utilized $Fe(CO)_5$ as the iron-containing catalyst precursor for the growth of SWNTs.[18] The process resulted in the attachment of iron oxide nanoparticles to one end of the nanotubes, allowing MR imaging. The constructs were imaged using MRI and NIR spectroscopy in cells. CNTs/iron oxide hybrids applied for in vivo MRI were also recently studied by Wu et al. in the form of MWNT-$Fe_3O_4$ hybrids.[19] The hybrids accumulated in lung, liver and spleen and the $T_2$-weighted MRI revealed significantly reduced signals in liver and spleen. Chen and the colleagues developed a 'layer-by-layer' approach to assemble CNTs/iron oxide hybrids with quantum dots for in vitro magnetic-fluorescence dual imaging.[20] There was also a study using carboxylated SWNTs containing traces of iron for in vivo MRI.[21] Recently, Yin et al. demonstrated an *in vitro* targeting effect of CNTs/iron hybrids conjugated to the tumour targeting ligand folic acid.[22] Targeted constructs accumulated more in folate receptor positive cells compared to the non-targeted counterparts and thus displayed a darker MR image.

Since SPION has been shown to be an effective MRI contrast agent, there have been studies to broaden the potential of iron oxide in biomedical imaging by merging with a radionuclide to combine MRI and SPECT/PET.[27–36] Such integration was often performed through polymeric coating which may not have desirable stability, especially in vivo.[31,32] A new approach has been introduced by de Rosales et al. using bisphosphonates (BPs) to link SPION with radionuclides.[33,35,36] With regards to the strong binding ability of BPs to the surface of SPION, radiolabelled-BPs were successfully conjugated to the iron oxide core and permitted quantitative biodistribution studies as well as dual SPECT/PET-MR imaging.[33,35,36]

In the present study, we have exploited this novel approach to synthesize magnetic yet radioactive MWNTs as dual MRI and SPECT contrast agents. To the best of our knowledge, this is the first study documenting the use of CNTs/iron oxide hybrids for dual MRI and nuclear imaging. In this work, the $R_2$* magnetic properties and the efficiency of radio-labelling SPION/MWNT hybrids were examined. In vivo experiments were performed to characterize the hybrids as multimodal SPECT and MRI contrast agents.

## 2. Results

### 2.1. Synthesis of SPION–MWNT Hybrids

The as-received MWNT materials were firstly purified by steam and HCl to remove some impurities, namely amorphous carbon, graphitic particles (carbon nanomaterials having few graphitic layers) and some metal particles. These metal particles, from the catalyst used for the growth of the MWNT, are covered by graphitic shells which inhibit their direct dissolution in an acidic media. Steam removed the amorphous carbon present in the samples and the graphitic shells covering the metal particles.[37] The removal of the amorphous carbon is essential to allow an efficient sidewall functionalization of the carbon nanotubes.[38] Purified MWNTs were then treated with nitric acid to introduce oxygen bearing functionalities (mainly carboxylic acid groups (–COOH)) onto the MWNT tips and sidewalls.[39,40] SPION–MWNT hybrids containing increasing amount of iron content were synthesized in situ by mixing the functionalized MWNTs with a precursor for the formation of the nanoparticles. It is known that when metal salts are dissolved in the presence of acid treated nanotubes, the metal ions interact strongly with the surface groups present onto the MWNTs.[41] Such interactions were expected to occur in our samples when mixing iron acetate (precursor) with the functionalised MWNTs, thus affording a homogeneous coverage of the iron atoms onto the surface of the MWNTs. Subsequently, the samples were thermally treated and left exposed to air thus resulting in the formation of the iron oxide nanoparticles.

### 2.2. Physicochemical Characterization of SPION–MWNT Hybrids

The amount of SPION present in the hybrids was quantitatively determined by thermogravimetric analysis (TGA) carried out under flowing air (**Figure 1**A). As shown in the

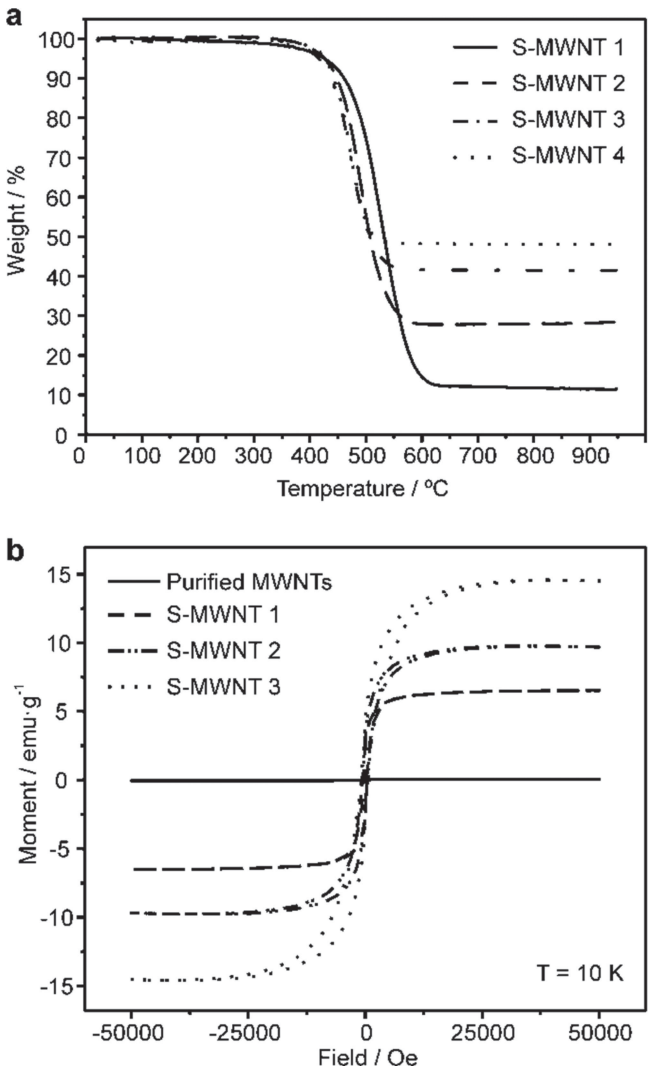


**Figure 1.** Physicochemical characterisation of SPION–MWNT hybrids. A) Thermogravimetric analysis of S-MWNTs in flowing air; B) Hysteresis loops of S-MWNT **1–3** at 10 K after subtracting the linear background; purified MWNTs were included for comparison.

TGA curves, oxidation of the samples took place at around 450 °C. Therefore, the residue obtained after the complete combustion of carbon atoms at 600 °C corresponded to the amount of iron oxide nanoparticles loaded onto the MWNTs. SPION–MWNT hybrids containing 11.5, 28.0, 41.5, and 48.0 wt% of SPION (assuming $Fe_2O_3$) were obtained and named S-MWNT **1–4** respectively from now on, where S refers to the superparamagnetic properties of the iron oxide nanoparticles deposited on the MWNTs. The superparamagnetic properties are described in the later section. S-MWNT **4** was found to be physically unstable in aqueous dispersions, as will be described later, thus was disregarded in further studies. Magnetic measurements at 10 K were performed to evaluate the effect of the increasing amount of SPION. Figure 1B shows the hysteresis loops for S-MWNT **1–3** and steam purified MWNTs which was included as a control. Purified MWNTs showed extremely weak magnetic signals, almost inappreciable in the figure, which was expected for samples with negligible catalytic impurities.[42] This was in agreement with TGA data under flowing air of the purified material that confirmed an almost unappreciable amount of residual metal catalyst (Figure S1). Samples with a metallic content below 1 wt% are dubbed as "high quality" in terms of catalyst content (impurities from the synthesis of the carbon nanotubes.[43] In contrast to purified MWNTs, a marked ferromagnetic behavior was observed for hybrids S-MWNT **1–3** at 10 K. As expected, samples with increasing amount of loaded SPION yielded higher saturation magnetization. Values for the saturation magnetization were measured as 6.5, 9.7, and 14.6 emu per total gram of sample (emu·$g^{-1}$) for S-MWNT **1–3** respectively.

### 2.3. Phantom MR Imaging and $R_2$* Relaxation Measurements

The transverse $R_2$* relaxation rates of S-MWNT **2-3** dispersed in 1% agar and 0.5% Pluronic F127 solution at different Fe concentrations were measured at 7 Tesla (7T). Although the hybrids studied here displayed good dispersibility using 1% Pluronic F127 solution before dilution with agar, phantom samples were prepared by dispersing the materials in agar to avoid the sedimentation of samples and thus achieve more accurate relaxation measurements. The same preparation and measurements using Endorem, a clinically approved SPION, were carried out for comparison. S-MWNT **1** with the lowest iron content was not investigated here since the dispersion was not ideal due to high sample concentrations required to achieve equivalent Fe amount to the other hybrids and thus for reliable MR imaging. **Figure 2**A shows MRI of Endorem (i) and S-MWNT **2-3** (ii-iii) at different concentrations at an acquired echo time of 5 ms. Some of the vials reported none or little signal due to fast signal decay effects when imaged at increased echo times. By sampling such signal shortenings, $R_2$* values were determined. The relaxation times of S-MWNT **2-3** and Endorem were plotted versus concentrations of iron (Figure 2B), reporting good linear correlations. The $r_2$* relaxivities were calculated as 343 $s^{-1}mM^{-1}$, 425 $s^{-1}mM^{-1}$ and, 325 $s^{-1}mM^{-1}$ for S-MWNT **2-3** and Endorem respectively. Endorem reported the lowest $r_2$* relaxivities while S-MWNT **3** showed the highest $r_2$* making it an MR appealing probe for $R_2$* and $R_2$ investigations.

### 2.4. Characterization of S-MWNT 3

Further characterization was performed for S-MWNT **3** since it was found to be the hybrid with the best $r_2$ relaxivity. **Figure 3**A,B and Figure S2 display transmission electron microscopic (TEM) images of S-MWNT **3** where SPION were shown along the backbone of the carbon nanotubes. High resolution TEM (HRTEM) analysis (Figure 3C) confirmed the presence of crystalline nanoparticles attached to the walls of carbon nanotubes. Electron diffraction analysis of these and other nanoparticles along with fast Fourier transform (FFT) simulations confirmed that the structure of the nanoparticles fit a cubic structure. The FFT pattern of one of the nanoparticles is shown as the inset in Figure 3C. Indexation of this pattern and its corresponding simulation are in good agreement with the [–233]

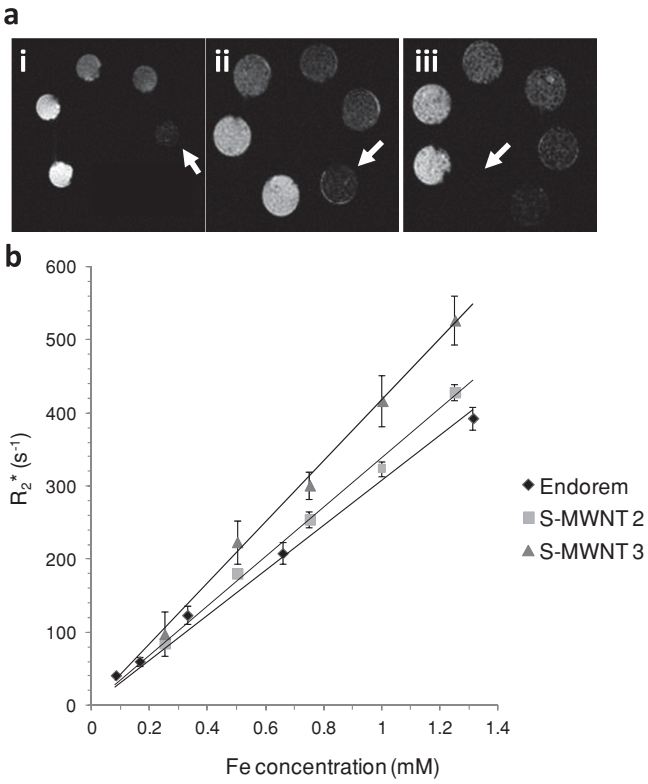


**Figure 2.** Phantom MRI studies. A) Phantom MR imaging of Endorem (i) and S-MWNT **2-3** (ii-iii). Samples are arranged clockwise from lowest (brightest) to highest (white arrows) iron concentration; B) $R_2$* relaxation time analysis as a function of Fe concentration. A 7 Tesla magnet was engaged for image acquisition. $r_2$* relaxivities of the hybrids were obtained from the different slopes. Results are presented as mean ± S.D. (n = 3).

zone axis. This allowed us to narrow the nature of the SPION to either $\gamma$-$Fe_2O_3$ or $Fe_3O_4$, and all other oxide possibilities can be excluded.

The size of SPION that decorated MWNTs was determined based on TEM images analysis. The diameter of about 200 SPION was measured and the resulting histogram is presented in **Figure 4**A. The majority of the SPION have diameters between 4–8 nm, with a mean value of 6.5 ± 4.0 nm. The presence of small particles was responsible for the low signal to noise ratio showing in the X-ray diffraction (XRD) pattern of the hybrid (Figure 4B). The observed peaks in Figure 4B could be assigned to those of carbon (pdf –powder diffraction file– 750444) from carbon nanotubes and to either maghemite ($\gamma$-$Fe_2O_3$; pdf 391346) or magnetite ($Fe_3O_4$; pdf 740748). No peaks for iron (II) acetate which was used as a precursor were observed indicating a successful decomposition by the thermal treatment. Further evidence for the complete decomposition of iron acetate was provided by TGA analysis performed under flowing nitrogen where no weight loss at low temperature is observed (Figure S3). The sharp drop at 710 °C for S-MWNT **3** was in good agreement with the percentage weight loss expected from the carbothermal reduction of the iron oxide nanoparticles by carbon (from the CNTs). Although the synthesis of the nanoparticles was performed under reducing conditions ($Ar/H_2$ mixture), the posterior exposition of the samples in air led to the complete oxidation of the nanoparticles. X-ray photoelectron spectroscopy (XPS) was performed to get further insight into the nature of the nanoparticles. A cumulative detailed scan performed over the Fe 2p region is presented in Figure 4C. The position, shape and width of the XPS peaks and the presence of the "shake-up" satellite structure at 719.3 eV is distinctive of the $\gamma$-$Fe_2O_3$ structure.[44]

In order to determine superparamagnetic properties of the SPION, hysteresis loops at 300 K were recorded. As shown in Figure 4D, no remnant magnetization was observed when there was no applied magnetic field, which is the typical behavior of a superparamagnetic material. Collectively, it is confirmed that the MWNTs were decorated with superparamagnetic $\gamma$-$Fe_2O_3$ nanoparticles (SPION).

### 2.5. Radio-Labelling Efficiency and Serum Stability Studies

Radio-labelling of SPION–MWNT hybrids was conducted as described previously using a functionalized bisphosphonate (BP) namely dipicolylamine-alendronate (DPA-ale) as a linker between SPION and the radioisotope $^{99m}Tc$[34] (**Scheme 1**). DPA-ale is described as BP in the following sections. To investigate the possible influence of iron content on the radio-labelling efficiency, pristine MWNT (p-MWNT)

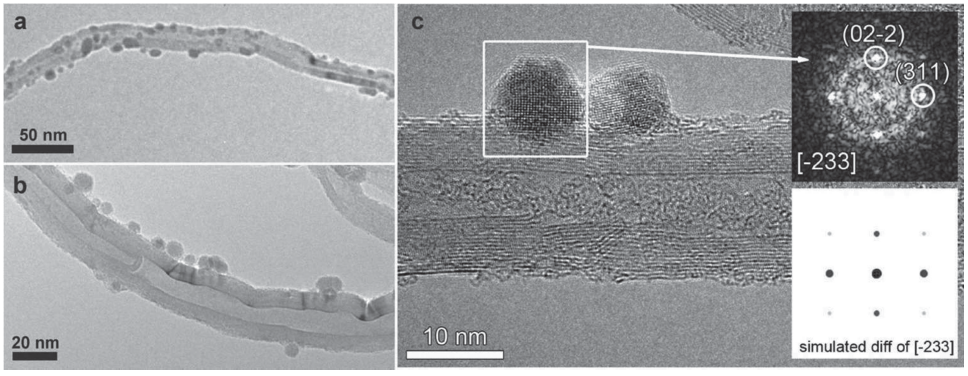


**Figure 3.** TEM analysis of S-MWNT **3**. A,B) TEM images at two different magnifications; and C) a high resolution transmission electron microscopy (HRTEM) image of S-MWNT **3**; the inset presents the diffraction pattern of a nanoparticle and the simulated diffraction pattern along the zone axis [–233].

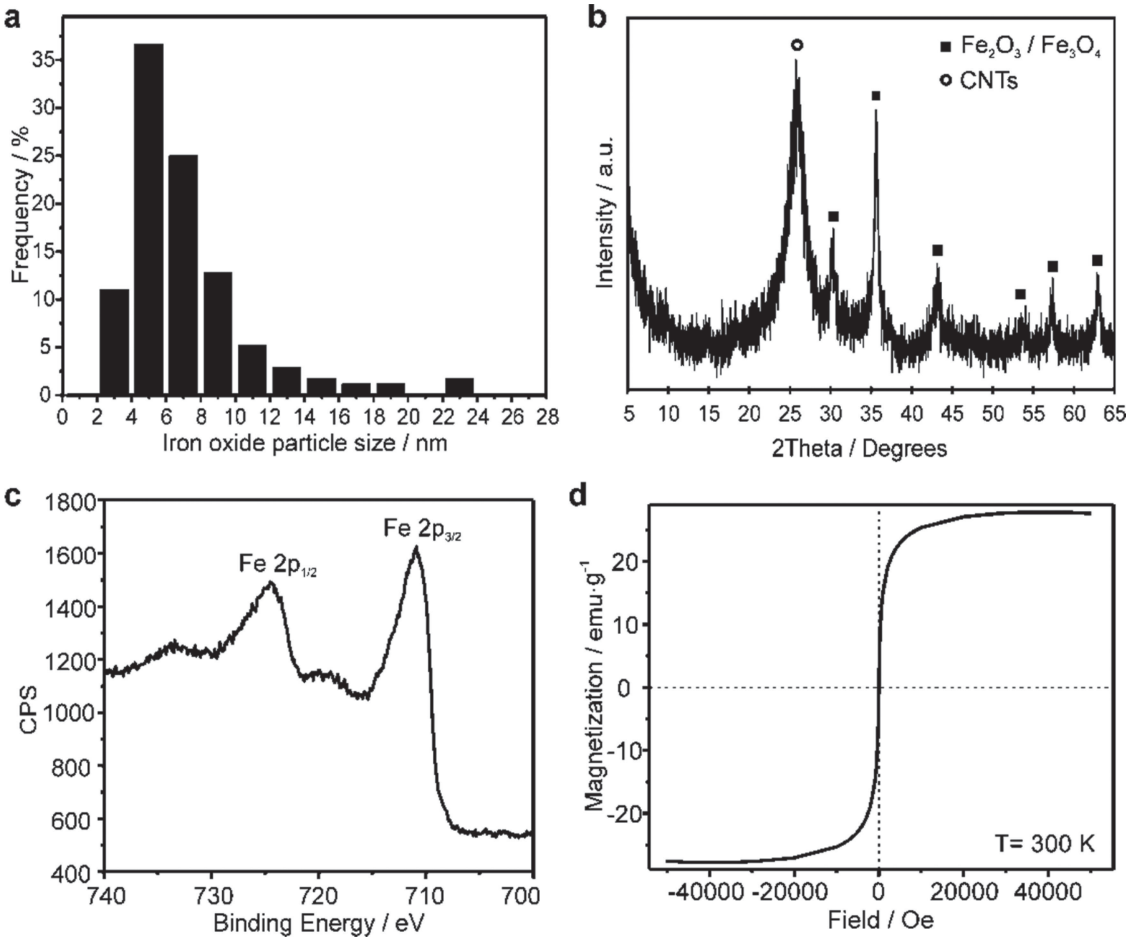


**Figure 4.** Characterization of the iron oxide nanoparticles decorating MWNTs. A) Histogram of the nanoparticle size, B) X-ray diffraction pattern, C) X-ray photoelectron spectroscopy, and D) hysteresis loops at 300 K.

without SPION and S-MWNT **1–3** with increasing iron contents were radio-labelled. As shown in **Figure 5**A, low radio-labelling efficiency was observed in p-MWNT in contrast to the S-MWNT hybrids where labelling yields were obtained above 57.5% ± 2.3. The low radio-labelling yield for p-MWNT could be due to non-specific adsorption of $^{99m}$Tc-BP to the graphitic backbone of CNTs. The best labelling efficiency was achieved for S-MWNT **2** and **3** with values of 82.5 ± 3% and 79.3 ± 3%, respectively. The results indicated that, as expected, the amount of iron content has an impact on the radio-labelling efficiency, and hybrids with higher SPION contents exhibited higher radio-labelling yields.

Stability studies were assessed by incubating the labelled hybrids in either human serum or PBS (50% final concentration) at 37 °C for 24 h. The results demonstrated high stability of all radio-labelled S-MWNTs in either human serum or PBS (Figure 5B). Most of $^{99m}$Tc was still bound to the hybrids (more than 90%) after 24 h incubation. Since S-MWNT **3** displayed the best radio-labelling yields and stability in serum, it was selected to be used in the subsequent dual in vivo imaging and organ biodistribution studies.

### 2.6. Whole Body 3D SPECT/CT Imaging of Mice Injected with $^{99m}$Tc-BP-S-MWNT 3

Whole body SPECT imaging in combination with computed tomography (CT) scanning was carried out to study the organ biodistribution of the radio-labelled $^{99m}$Tc-BP-S-MWNT **3** (4 MBq, 50 µg hybrid) or $^{99m}$Tc-BP (5 MBq) alone at 30 min, 3 h, and 24 h after i.v. injection in mice. As shown in the bottom panel in **Figure 6**A, $^{99m}$Tc-BP was mainly detected in bone at the early time points (<30 min and 3 h) which is expected due to the high affinity of bisphosphonates to bone minerals.[34] Accumulation in kidney and bladder was detected in mice treated with $^{99m}$Tc-BP within 30 min after injection suggesting rapid renal clearance. $^{99m}$Tc-BP-S-MWNT **3**, however, showed predominant accumulation in lung, followed by liver and spleen (top panel in Figure 6A) within 30 min after injection. The signals in the liver remained constant after 4 h while a clear reduction in lung accumulation was observed over the first 4 h. Similar to $^{99m}$Tc-BP, a small fraction was detected in the bladder after 30 min indicating rapid clearance for some $^{99m}$Tc-BP-S-MWNT fractions. Low SPECT signals were detected

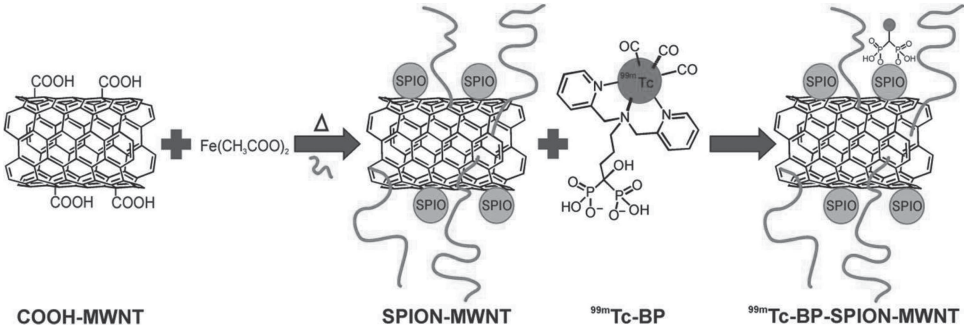


**Scheme 1.** Radio-labelling of SPION–MWNT hybrids with technetium-99m ($^{99m}$Tc) via a linker. The Radio-labelling was conducted using $^{99m}$Tc-dipicolylamine-alendronate ($^{99m}$Tc-DPA-ale, referred to $^{99m}$Tc-BP thereafter) as described previously.[34]

in both mice at 24 h post administration (Figure S5). The 'virtual' loss of radioactivity is most likely due to the decay of the radionuclide (half-life for $^{99m}$Tc, 6 h) as is the case of short, half-lived radioisotopes. Therefore, post-mortem $\gamma$-scintigraphy was conducted in parallel to SPECT/CT imaging to assess quantitatively the organ biodistribution of the hybrids over time.

### 2.7. Organ Biodistribution and Blood Clearance Profile of $^{99m}$Tc-BP-S-MWNT 3 in Mice After i.v. Injection

Organ biodistribution of $^{99m}$Tc-BP-S-MWNT **3** or $^{99m}$Tc-BP alone in major mice organs was examined at 1, 4, and 24 h after i.v. injection. The results correlated well with the SPECT images that lung, liver, and spleen were the major organs of accumulation (Figure 6B and Figure S6A). In view of organ biodistribution over time, the hybrid seemed to retain in liver and spleen tissues up to 24 h post injection as the percentage of injection dose (%ID) per gram tissue remained constant (Figure 6B). Despite the reduction in %ID per gram lung tissue observed, substantial amount of the hybrid (i.e., 12.8% ± 1.9 ID/organ) was still detected in the lung after 24 h.

On the contrary, a markedly different organ biodistribution profile was observed for $^{99m}$Tc-BP. A typical bisphophonate pharmacokinetics was featured with profound accumulation in the bone and minimal exposure to other tissues (Figure 6C and Figure S6B). The results indicated successful conjugation of $^{99m}$Tc-BP to SPION-MWNT hybrids, as shown by the altered organ biodistribution pattern in vivo.

Different blood clearance profiles were found for $^{99m}$Tc-BP and $^{99m}$Tc-BP-S-MWNT **3** (Figure 6D). Despite less than 2.9% ± 0.3 of ID was measured in blood at 30 min after i.v. injection in the case of the hybrid, the amount of $^{99m}$Tc-BP detected at the earliest time point (2 min) was approximately 3 times higher than that of $^{99m}$Tc-BP-S-MWNT **3**.

### 2.8. In Vivo MR Imaging and liver R2* Relaxation Time Measurements

Since SPECT imaging demonstrated accumulation of the hybrid in the reticuloendothelial system (RES, e.g., liver and spleen), MRI was engaged in the liver in order to verify the correct multimodality effect of the hybrid. **Figure 7**A shows axial

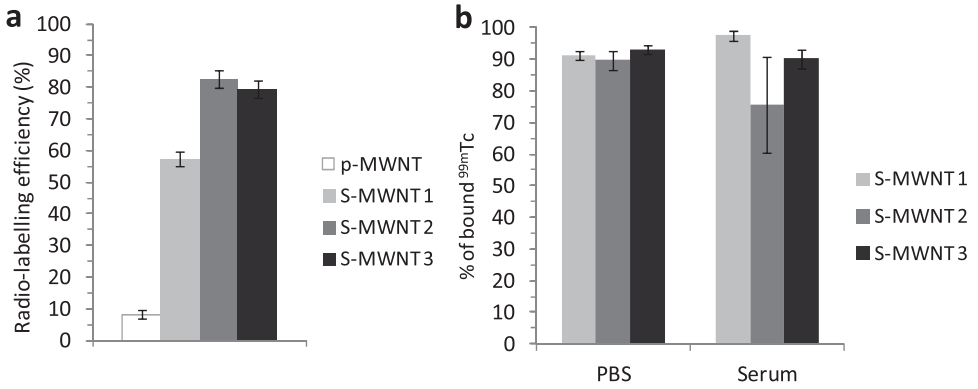


**Figure 5.** Radio-labelling efficiency and stability of SPION–MWNT hybrids. A) Radio-labelling efficiency of pristine MWNT (p-MWNT) and S-MWNT **1–3**. Hybrids dispersed in 1% Pluronic F127 solution at 1 mg/mL concentration were mixed with $^{99m}$Tc-BP at 37 °C for 30 min. Radio-labelling efficiency was estimated by measuring the radioactivity in the pellets (bound $^{99m}$Tc-BP) and supernatants (unbound $^{99m}$Tc-BP) of the samples after centrifugation at 17 000 rcf for 30 min. B) Serum (50%) and PBS stability studies of radio-labelled S-MWNT **1–3** after 24 h incubation at 37 °C.

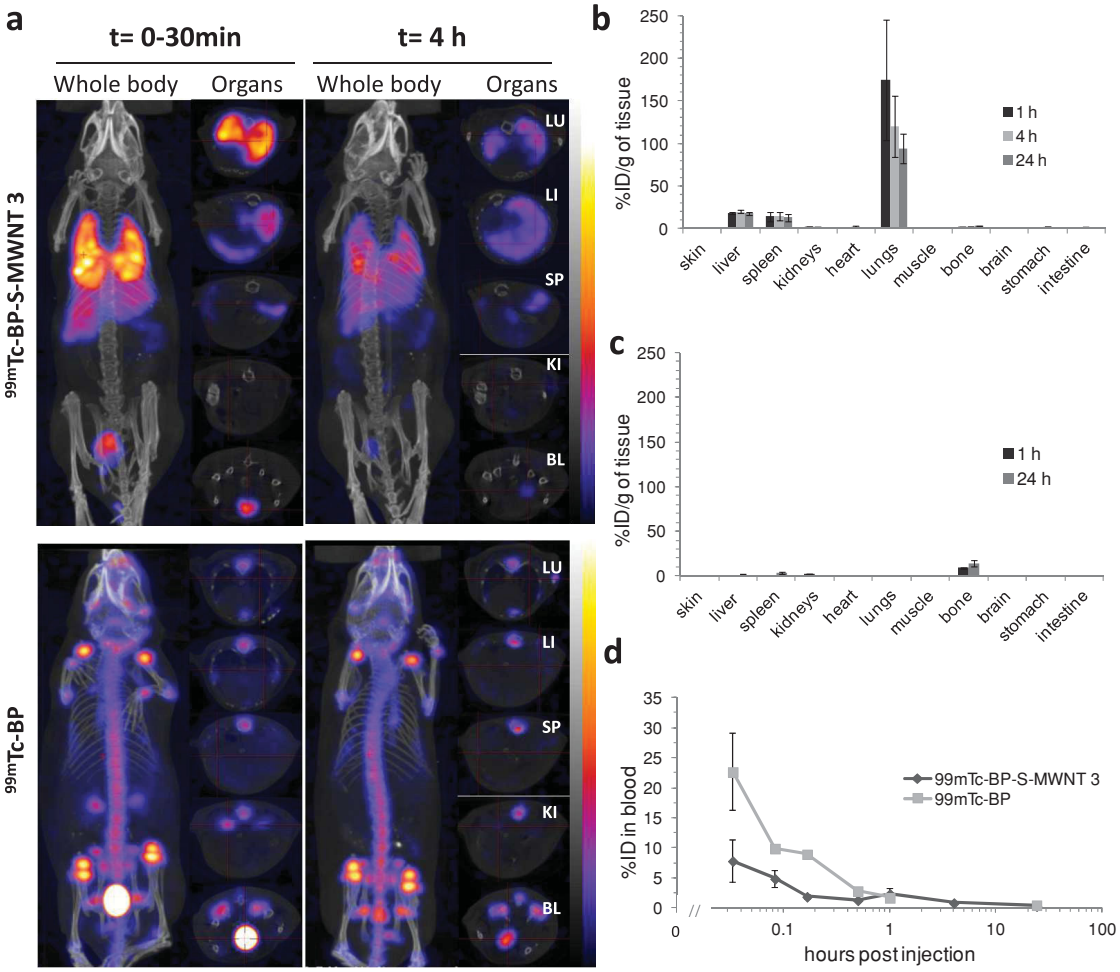


**Figure 6.** In vivo SPECT/CT and organ biodistribution studies following i.v. injection of $^{99m}$Tc-BP-S-MWNT **3** or $^{99m}$Tc-BP. A) Whole body 3D SPECT/CT imaging; B) organ biodistribution of $^{99m}$Tc-BP-S-MWNT **3** and; C) $^{99m}$Tc-BP. D) Blood clearance profile of $^{99m}$Tc-BP-S-MWNT **3** and $^{99m}$Tc-BP. Cross sections in (A) were taken at lung (LU), liver (LI), spleen (SP), kidney (KI) and bladder (BL). Results are expressed as mean ± S.D. (n = 3).

liver images at different acquisition echo times against Fe concentration (mg/kg) of the hybrid. Like the results obtained in phantoms, MRI signals were darkened over time and the decay effects appeared faster upon increasing iron dosage. The $R_2$* relaxation rate was plotted in Figure 7B accordingly. The measured in vivo $R_2$* relaxation rates from liver increased almost linearly in relation to the injected Fe doses.

### 2.9. Microscopic Examination of S-MWNT 3 in Tissues

To examine the presence of the hybrid in tissues after i.v. injection, tissues of lung, liver and spleen were sampled at various time points up to 30 days and stained by either Perls stain or Neutral Red stain. Mice were administered 400 µg of S-MWNT **3** (5.8 mg Fe/kg), a much higher dose than that used in biodistribution and SPECT studies, in order to be able to detect the hybrids by histological examination.

Perls stain is commonly used to demonstrate iron in tissues in histology. As shown in **Figure 8**A, blue staining indicating the presence of iron (shown by arrows) was observed in the three organs at 24 h, 7 days, and 30 days. Spleen injected with the vehicle alone (1% Pluronic F127 in PBS) lacking the SPION was shown to be the most positive to Perls stain. Moreover, a gradual increase in iron content over time was noted in spleen up to 30 days after injection and more iron was found in the red pulp region than white pulp. Red blood cells, which normally reside in the red pulp were stained with creamy brown colour (Figure 8A). On the contrary, the amount of iron in liver and lung declined over time since very few blue-stained regions were observed after 30 days. In comparison, no iron (blue stain) was observed in Pluronic F127 liver tissues. It was also noted in the liver sections that more blue stain appeared in the cytoplasm of Kupffer cells compared to hepatocytes. This advanced uptake might be due to the phagocytic nature of Kupffer cells.

Separate tissue sections were then stained with Neutral Red as a counter stain to enable visualisation of the MWNTs.[45,46] The results were in agreement with Perls stain that MWNTs (shown by arrows) showed the same pattern as iron in lung and liver with reduction observed in these tissues over time

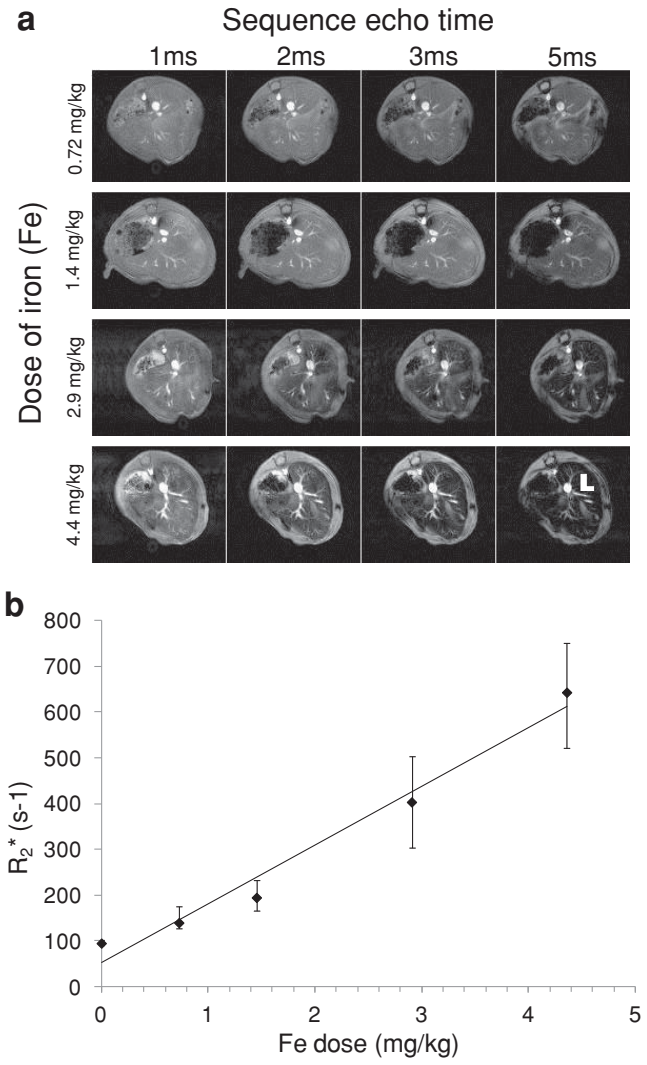


**Figure 7.** In vivo $T_2$*-weighted MR studies. A) MR images of mouse liver 48 h after injection with various doses of S-MWNT **3** over time; B) $R_2$* relaxation rate measurements. L: liver.

(Figure 8B). MWNTs presented in spleen were also found in the red pulp region. Few batches of MWNTs remained in lung at 30 days and were shown as large aggregates.

In summary, a good correlation was demonstrated in the organ biodistribution profile between the MWNTs and iron under microscopic examination, indicating a good stability of SPION-MWNT in vivo. Moreover, additional studies using TEM were carried out to confirm the integrity at the nanoscale level.

### 2.10. TEM Studies of Mice Organs

To confirm the co-localisation of SPION and MWNT at ultrastructural levels, TEM examination for tissues sampled at 24 h after i.v. injection of 400 μg of S-MWNT **3** (5.8 mg Fe/kg) was carried out. Liver and spleen were chosen here as they showed high accumulation of the hybrid. Interestingly, the results confirmed uptake of the hybrid not only in kupffer cells but also in hepatocytes of the liver. A series of TEM images were taken for hepatocytes at different magnifications (**Figure 9**A,B). Hepatocytes are recognised by the presence of a substantial number of mitocondria. The hybrids were often identified within vesicles. Both SPION and MWNTs were observed in the same endocytic vesicle, suggesting the uptake of MWNTs and SPIOs as an intact hybrid. SPION were shown as electron-dense particles (dotted black arrows) while MWNTs were confirmed with their tubular structures (solid black arrows). At 24 h, SPION were found dissociated from the MWNTs perhaps due to the low pH of endocytic vesicles. Figure 9C,D show a kupffer cell (white dotted line), the professional macrophage cells located in liver, where a similar pattern to that of hepatocytes was observed. TEM images of spleen are shown in Figure 9E,F. Again, SPION and MWNTs were observed in the same endocytic vesicles with some SPION being detached from MWNTs while some remained intact.

Co-localisation observed within the same endocytic vesicles indicated that the hybrids were stable enough to be able to pass through many biological barriers after i.v. administration, enter the same organ and to be internalised as intact hybrids by the same cell within the same endocytic vesicle.

### 2.11. Histological Examination by H&E

Histological analysis was carried out on H&E stained paraffin embedded tissue sections sampled at various time points up to 30 days after i.v. injections of 400 μg S-MWNT **3** (5.8 mg Fe/kg) (**Figure 10**). No significant histological changes were observed in lung, liver and spleen compared to untreated tissues. Tissues taken from animals treated with 1% Pluronic F127 solution alone were also examined and the results confirm no abnormalities induced. Such results indicated the biocompatibility of the hybrid in vivo under the conditions tested.

## 3. Discussion

The future of diagnostic applications lies on the use of multimodal approaches by combining different imaging modalities to achieve an accurate diagnosis in cancer, cardiovascular disease and other disorders. These attempts are to integrate the advantages of each imaging tool and compensate their limitations. The best example is the combination of SPECT/PET with MR or X-ray CT. As mentioned previously, the new generation of multimodal imaging equipment is the combination of MRI with SPECT/PET in which pioneer instruments designed for MR/PET hybrid imaging for human have been setup recently.[47] As a result, the collected imaging outcomes would contain excellent tomography from MRI (resolution down to 50–250 μm) and great sensitivity achieved by SPECT/PET ($10^{-10}$ to $10^{-12}$ mol/L).[14] Another important reason for these imaging techniques being used widely in the clinic is attributed to their unlimited penetration depth. This overcomes the major disadvantages of optical imaging techniques, particularly fluorescence detection, which is highly restricted to the location of

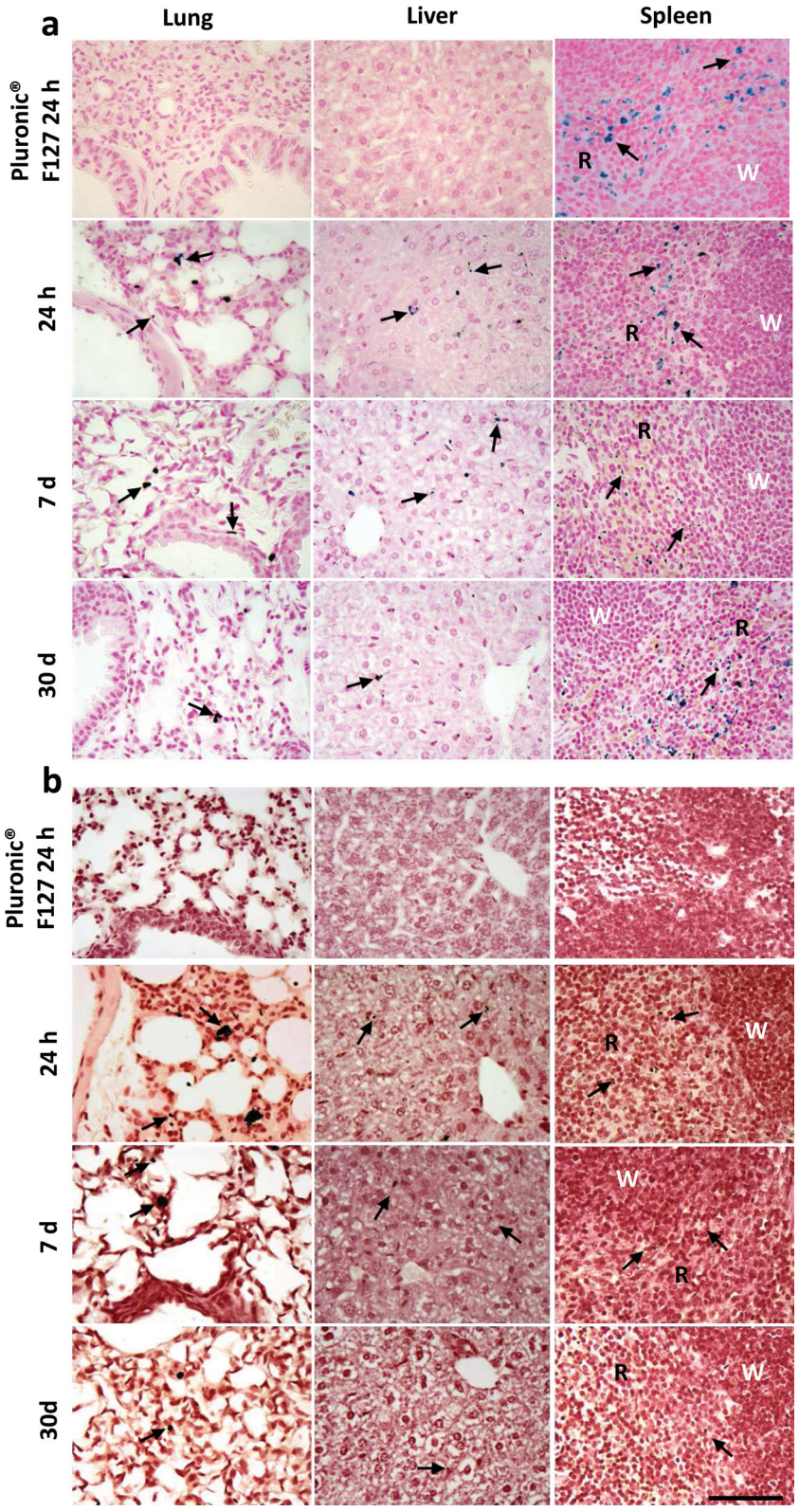


**Figure 8.** **M**Microscopic examination of liver, lung and spleen sections of C57/Bl6 mice injected with S-MWNT **3.** Animals were injected with the vehicle alone (1% Pluronic F127) or 400 µg of the hybrid (5.8 mg Fe/kg). Selected organs were sampled at 24 h, 7 days, and 30 days after injection and stained with A) Perls staining or B) Neutral Red staining. Arrows in (A) point to the presence of iron (blue colour) and arrows in (B) point to the presence of carbon nanotubes (black dots) in the tissue sections. W: the white pulp region of spleen; R: the red pulp region of spleen. The scale bar corresponds to 50 µm.

the imaging targets, the type of light source used (e.g., laser wavelength), and intrinsic tissue properties (e.g., tissue absorption and scattering).[12]

A recently published study reported the synthesis of CNT/iron oxide hybrids by ligand exchange or click chemistry approaches.[48] In the current study, SPION–MWNT hybrids were prepared by in situ generation. MWNTs were treated with acid to introduce oxygen bearing functionalities on the sidewalls and tips. The decoration of steam purified MWNTs (without the oxygen bearing functionalities) with iron oxide nanoparticles was also carried out as a control. The functionalization of the nanotubes was found to play a key role in providing a homogenous decoration with the nanoparticles. A more uniformed coverage of iron oxide nanoparticles was achieved when employing functionalized MWNTs compared to using the nanotubes lacking oxygen-containing functionalities. The use of iron acetate as a precursor was exploited for the formation of the iron oxide nanoparticles. The procedure involved thermal annealing at high temperature, resulting in the formation of nanoparticles with high crystallinity as confirmed by HRTEM. To determine the degree of nanoparticle loading, TGA under flowing air was performed. As appreciated in the TGA curves (Figure 1A and Figure S1), steam purified MWNT started to oxidize under flowing air at higher temperature (600 °C) than the S-MWNT **1–3** samples with oxidization starting at about 450 °C. The decrease in the onset of combustion temperature, by about 150 °C, was due to the presence of inorganic nanoparticles in the samples. This phenomenon has been observed in samples of carbon nanotubes containing different inorganic materials.[49] Further characterization studies were carried out using HRTEM and XRD. HRTEM allows direct imaging and analysis of nanostructures and provides structural information down to the atomic scale. HRTEM analysis verified the presence of single-phase crystalline iron oxide nanoparticles and discarded the presence of core-shell nanoparticles (Figure 3C) and the diffraction peaks shown in XRD also denoted the presence of carbon and $Fe_2O_3/Fe_3O_4$ in the bulk sample (Figure 4B). However, both $\gamma$-$Fe_2O_3$

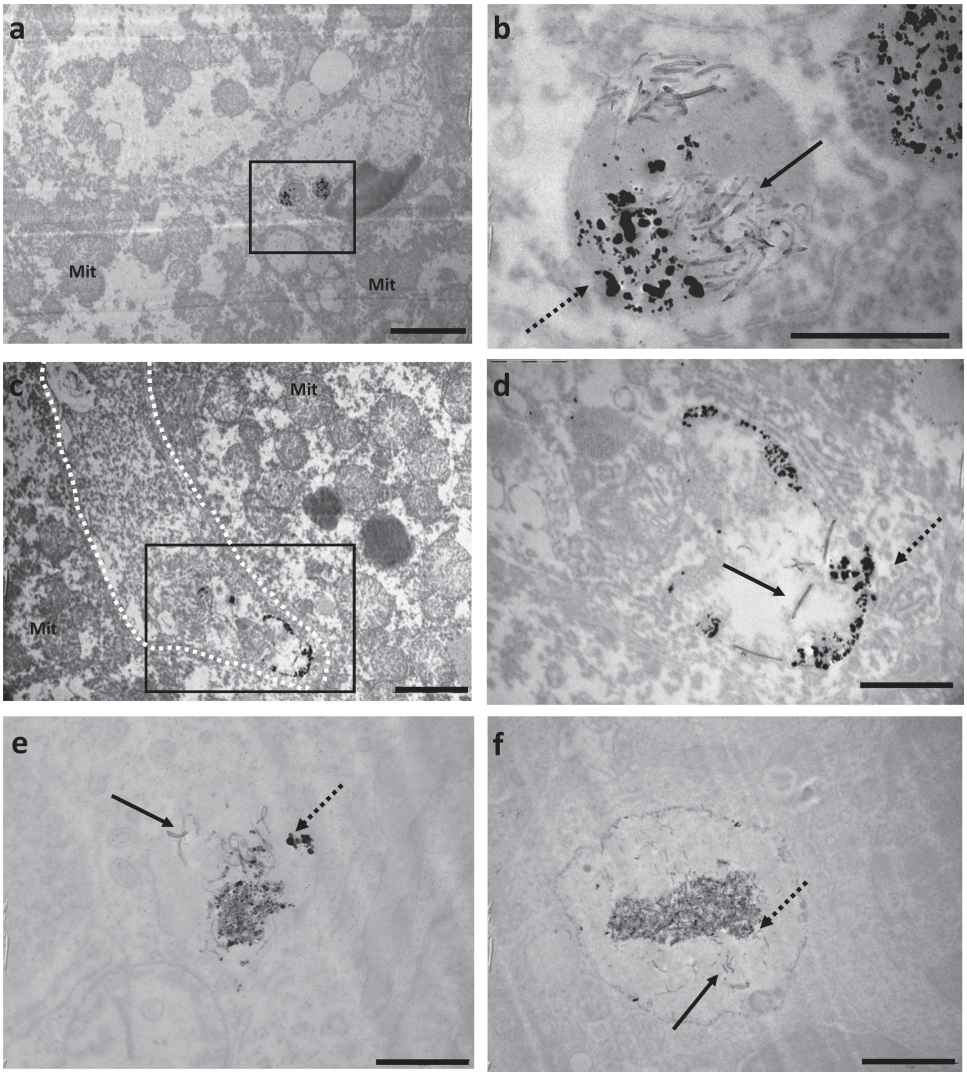


**Figure 9.** TEM micrographs of liver and spleen sections from animals injected with S-MWNT **3** at 24 h. Animals were injected with 400 µg of S-MWNT **3** (5.8 mg Fe/kg) via a tail vein. Organs were excised, fixed in 3% glutaldehyde in 0.1 M cacodylate buffer, and sectioned for TEM. The presence of S-MWNT was identified in hepatocytes (A,B) and kupffer cells outlined in (C,D) and spleen (E,F). B,D) Higher magnification images from the inset rectangles in (A) and (C), respectively. Dashed arrows point SPION and solid arrows point MWNTs. Mit: mitochondria. Bars are 2 µm in (A) and (C), 0.5 µm in (B) and (D), and 1 µm in (E) and (F).

and $Fe_3O_4$ possess spinel structures that belong to the Fm-3d space group (cell parameter a($\gamma$-$Fe_2O_3$) = 8.351 Å; a($Fe_3O_4$) = 8.384 Å) and their bulk saturation magnetization are also similar (Ms($\gamma$-$Fe_2O_3$) = 87 emu $g^{-1}$; Ms($Fe_3O_4$) = 92 emu $g^{-1}$).[50] It also must be taken into account that the saturation magnetization of small nanoparticles is usually smaller than that of the bulk[51] which prevents the elucidation of the particle type from the performed magnetic measurements. Thus, it was not possible to elucidate the nature of the SPIOs based on diffraction studies and magnetic measurements. The nature of the iron oxide nanoparticles in the SPIO-MWNT hybrids studied was therefore investigated by XPS and identified to be $\gamma$-$Fe_2O_3$ (Figure 4C). Magnetic measurements at 300 K confirmed that the $\gamma$-$Fe_2O_3$ nanoparticles possessed a superparamagnetic behaviour. Such temperature is close to room temperature, i.e., administration condition therefore it was necessary to confirm that no remnant magnetization is present when the magnetic field is removed at such temperature.

Phantom and in vivo MRI of S-MWNT hybrids were both conducted in this study. An intensive exploration of the $R_2$* relaxation rate was carried out by imaging phantom samples containing different amount of iron prepared in 1% agar and 0.5% Pluronic F127 solution (Figure 2A). S-MWNT **2** containing 28 wt% SPION exhibited a similar $r_2$* relaxivity to Endorem, and S-MWNT **3** with increased SPION contents displayed a greater value than Endorem (Figure 2B). The phantom study reported $r_2$* relaxivities of Endorem which appeared to be higher than the values published in some other $r_2$ studies.[52,53] Such discrepancies are related to several factors. Firstly, $R_2$* values reflect magnetic susceptibility

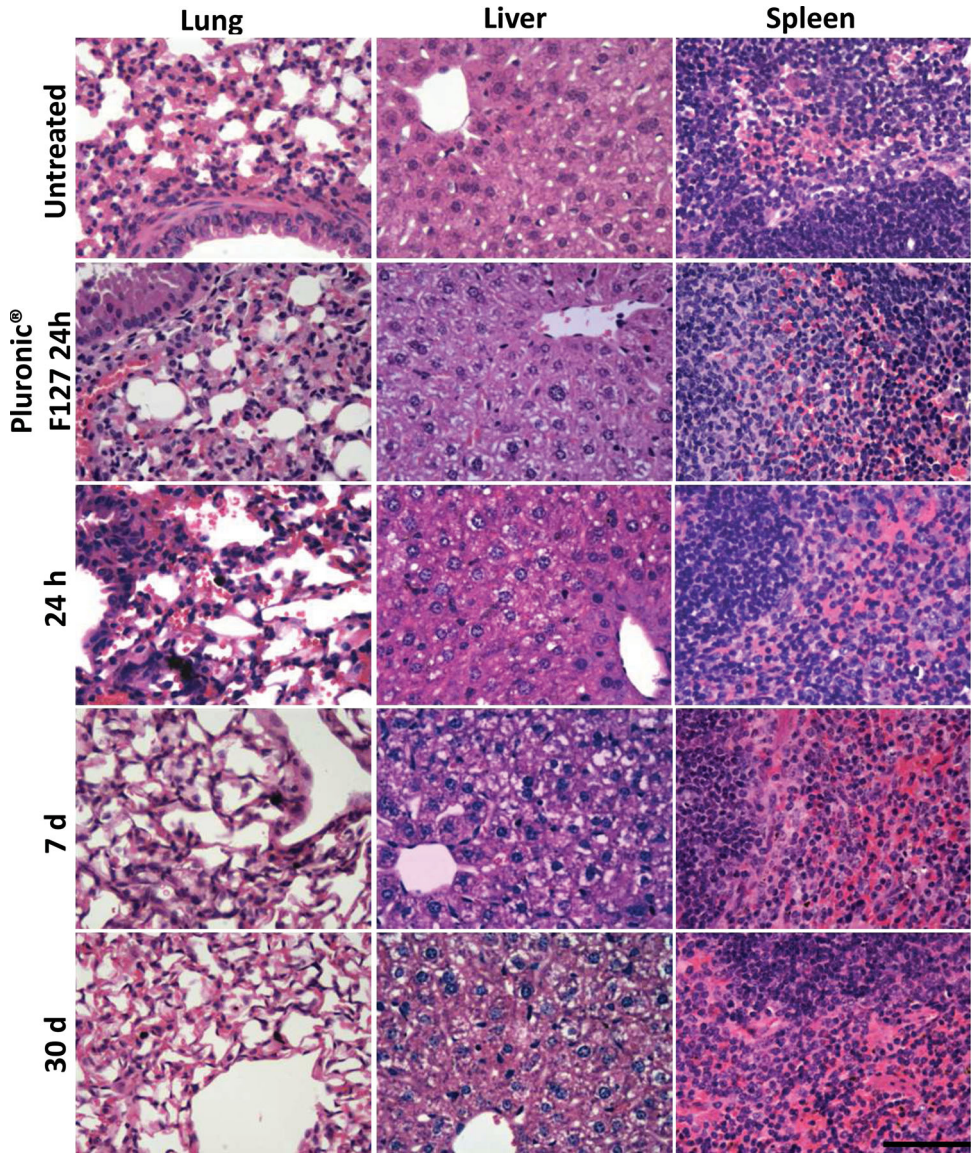


**Figure 10.** Histological examination of liver, lung, and spleen sections of C57/Bl6 mice injected with S-MWNT **3.** Animals were i.v. injected with 400 µg of the hybrid (5.8 mg Fe/kg). Organs were sampled at 24 h, 7 days, and 30 days, fixed, paraffin embedded and sectioned for H&E staining. Animals injected with 1% Pluronic F-127 were included as controls (at 24 h). The scale bar corresponds to 50 µm. No histological abnormalities were observed in all the organs examined up to 30 days.

effects which are largely avoided when engaging $R_2$ sequences. $R_2$* and $R_2$ are significantly different at high magnetic fields making it difficult to compare. Although $R_2$ is a more clinically relevant parameter than $R_2$*, the latter provides higher sensitivity at high fields making it an ideal tool for iron oxide probes investigations. Secondly, the use of agar most probably speed up phantom signal decay thus enhancing $r_2$* values. In fact, when investigating Endorem in water at 7 T, a $r_2$* value of 211.18 $s^{-1}mM^{-1}$ was obtained which agreed with what was reported in literature[54] (Figure S4). It also should be mentioned that the relaxivity patterns observed when engaging $R_2$* techniques should be similar to that observed when engaging $R_2$ techniques, making, in our case, the S-MWNT **3** highly relevant to in vivo clinical studies. Most importantly, high $r_2$* relaxivity of S-MWNT **3** implies that lower concentrations of the hybrids were required to achieve signals similar to that of Endorem. Liver $T_2$*-weighted MR imaging demonstrated time-dependent and concentration-dependent darkening in liver signals (Figure 7A) and an almost linear $R_2$* relaxation rate was obtained (Figure 7B). Higher relaxation effects were observed in our in vivo liver experiment when compared to two previously reported studies that utilised an equivalent amount of injected Fe.[19,55] A reduction of 60% in $R_2$* was seen up to 5 h after injection of 2.5 Fe mg/kg compared to 69% reduction value obtained in our study at the 48 h imaging time point.[19,55] In the second study, a reduction of 40% (at 2 h) at the dose of ~2.8 mg Fe/kg was measured compared to 76.5% obtained in our study at the same dose (at 48 h).[19,55] Despite the different

imaging time points which do not allow a direct comparison to be performed, the results showed S-MWNT **3** enhanced liver MRI contrast and confirmed S-MWNT **3** to be suitable as a negative contrast agent.

As far as this study is concerned, this is the first study proving the bimodal MRI/SPECT imaging using SPION-CNT hybrids. Better radio-labelling efficiency was obtained for S-MWNT **2-3** in contrast to S-MWNT **1** with lower SPION content (Figure 5A). This confirmed the radio-labelling approach which introduced $^{99m}$Tc-labelled BP to the SPION available on the carbon nanotube surface as opposed to non-selective adsorption of the radio-isotope to the MWNTs. Approximately, 80% labelling efficiency was already obtained for S-MWNT **2** while no enhancement in radio-labelling was achieved in S-MWNT **3** despite of the 1.5 fold increase in iron content of the latter.

The results from SPECT/CT and organ biodistribution studies revealed most of the S-MWNT **3** accumulated in lung, liver and spleen (Figure 6). SPION is known to be taken up by liver and spleen (RES) hence it has been widely used to detect liver diseases by enhancing the negative MRI signals.[56] The prolonged uptake of CNT/iron oxide hybrids in lung has been reported.[19] The lung accumulation may be also due to their tubular and long structure. Long fiber particles tend to cause pulmonary toxicity and fibres with the length longer than 10 μm were reported carcinogenic.[57] The mean length of the MWNTs was measured around 2 ± 1.8 μm (Figure S1) and no histological abnormality was observed from different mice tissues treated with S-MWNT **3** up to 30 days. In a previous study, no physical abnormalities were detected after biochemical analysis of serum and urine samples of mice treated with various MWNTs with the length between 0.5 and 2 μm.[58] Preliminary in vitro cytotoxicity of S-MWNT **3** has been assessed using the mouse macrophage cell line J774 and no significant toxicity was measured at concentrations up to 100 μg/mL after 24 h incubation (unpublished data). Work is currently being undertaken to investigate and compare the MR properties of S-MWNT hybrids with different lengths in vitro and in vivo.

The reduction in S-MWNT **3** accumulation in lung and liver over time was confirmed by microscopic examination of the tissue sections stained with Perls stain and Neutral Red to detect the presence of iron oxide or MWNTs respectively (Figure 8). Unlike lung and liver, contradictory results were obtained in spleen sections following two staining methods where an increase in Perls stain-positive regions were captured up to 30 days while a reduced level of MWNTs was observed in Neutral Red stain. Iron stains were mostly found in the red pulps of spleen. With this regard, spleen is one of the iron storage organs in the body and therefore the red pulps are often Perls stain-positive. Therefore, the blue stains in spleen could be attributed to the iron from S-MWNT hybrids or the natured iron resulted from heme oxidation from dead red blood cells.

TEM examination was further carried out for observation of S-MWNT hybrids in tissues at ultra-structural scale. The observation of SPION-CNT hybrids in vitro by TEM has been reported previously.[48] Prostate cancer cells were incubated with the hybrids for 20 h and TEM images revealed their localisation in endosomes/lysosomes as bundles or individual tubes. Iron oxide nanoparticles were still attached with CNTs at this time point after cellular internalisation. In another study, Wu et al. have used TEM to validate the presence of MWNT/iron oxide constructs in tissues at 4 h after injection.[19] In the present study, more detailed information on cellular localisation of S-MWNT hybrids was disclosed in which co-localisation of SPION and MWNTs within the same endocytic vesicles was clearly observed in spleen cells, liver hepatocytes and kupffer cells at 24 h after injection (Figure 10). The results provided sufficient evidence of the in vivo stability of S-MWNT oxide hybrids so that they were taken up by the same cells as intact hybrids after intravenous injection. The detachment of SPION from MWNTs was also observed which might be due to the acidic environment of these vesicles.

As mentioned previously, CNTs have been developed for biomedical imaging applications[7] and we have also radio-labelled CNTs with Indium-111[45,59] or filled Iodine-125 inside the tube[46] for in vivo imaging and biodistribution studies. The current study presented $^{99m}$Tc-labelled SPION-MWNT hybrids as dual MRI and SPECT contrast agents for the first time. The beauty of the design in this construct is the ease in preparation forming a stable construct capable of MRI and SPECT imaging upon reaction with a BP derivative. The BP derivative could be altered so that different radio-isotopes can be utilized[36,60] allowing for SPECT or PET imaging, both considered to be clinically very important modalities in disease diagnosis, staging and monitoring. The current study certainly assures a new prospect for CNTs application in the biomedical imaging field.

## 4. Conclusions

The present study has developed novel radio-labeled iron oxide nanoparticle decorated multi-walled carbon nanotubes (SPION–MWNT) hybrids for dual MR and SPECT imaging. Efficient and homogeneous loading of SPION were achieved via in situ generation, followed by thorough characterizations of physiochemical and magnetic properties of the prepared hybrids. In MRI studies, the resulting SPION–MWNT showed reduction in T2* signals in both phantom and the liver in vivo which was equivalent in efficacy to a clinically approved MRI contrast agent. Radio-labeling of SPION–MWNT with $^{99m}$Tc through a functionalized bisphosphonate was reported, permitting in vivo 3D whole body SPECT/CT imaging and organ biodistribution profiling quantitatively. The TEM observations of SPION and MWNT co-localizing intracellularly in the same vesicles in liver and spleen tissues denoted the in vivo stability. No organ abnormality was found histologically up to 30 days post-adminisitration indicating a good biocompatibility of the hybrids. Findings from this work demonstrated the capability of SPION–MWNT hybrids to be used in dual-modality MR-SPECT imaging thus broadening CNT applications in the biomedical imaging field.

## 5. Experimental Section

*Materials*: Chemical vapour deposition multi-walled carbon nanotubes (MWNTs) were supplied as a dry powder (Thomas Swan & Co. Ltd, UK)

with an external average diameter of 10–12 nm (information provided by the supplier). Iron acetate (III), human serum from human male AB plasma, Pluronic F127, agar, 10% neutral buffered formalin, and Perls stain kits were purchased from Sigma-Aldrich (Sigma- Aldrich, UK). Endorem was obtained from Guerbet (Guerbet Laboratories, UK). Dipicolylamine-alendronate (DPA-ale or BP) and $^{99m}$Tc -BP were synthesized as previously reported.[27] Na[$^{99m}TcO_4$] in physiological saline was obtained from a $^{99}$Mo/$^{99m}$Tc generator at the Radiopharmacy at Guy's and St Thomas' Hospital NHS Trust, London, UK. Radioactivity in samples was measured using a CRC-25R dose calibrator (Capintec, USA) or a 1282 CompuGamma gamma counter (LKB Wallac, PerkinElmer, USA). [$^{99m}$Tc $(CO)_3(H_2O)_3]^+$ was synthesized using Isolink kits (Mallinckrodt Medical B.V., St. Louis, MO, USA). C57/Bl6 female mice aged 6–8 weeks were used throughout the in vivo studies and were obtained from Harlan Laboratories. Isoflurane for anaesthesia was purchased from Abbott (IsoFlo, Abbott Laboratorie Ltd, UK) and pentobarbital sodium used for lung inflation fixation was from Merial (Euthatal, Merial Animal Health Ltd, UK). For sample preparation for histological and TEM examination, xylene, ethanol, and sodium cacodylate were purchased from Fisher Scientific, DPX used for mounting was obtained from VWR International Ltd, EM grade glutaldehyde was from Merck, and Araldite CY212, tris(dimethylaminomethyl)phenol (DMP30) dodecenyl succinic anhydride (DDSA) were purchased from Agar Scientific.

*Synthesis of SPION–MWNT Hybrids*: The as-received MWNTs were purified by steam following a previously reported protocol.[30] Briefly, MWNTs were ground with an agate mortar and pestle until a fine powder was obtained. Next, the MWNT sample was spread inside a silica tube (about 40 mm in diameter) which was then introduced into a furnace alumina tube. Steam was introduced by bubbling argon (150 mL min$^{-1}$) through a flask containing hot distilled water (98 °C). The whole system was initially purged with argon for 2 h to ensure the complete removal of oxygen, before heating the furnace to 900 °C during 1.5 h to allow the purification of the material. The solid powder was collected and treated with 6 M HCl to remove the now exposed metal nanoparticles.[33] The purified MWNTs were collected by filtration through a 0.2 µm polycarbonate membrane and thoroughly washed with water until pH neutral. The purified MWNTs were then functionalized by refluxing with 3 M $HNO_3$ for 45 h, resulting in the introduction of carboxylic acid groups (–COOH) onto the MWNT tips and side walls.[32] The functionalized MWNTs (*f*-MWNTs) were collected by filtration and washed with water until neutral pH was achieved.

Decoration of the MWNTs with SPION was carried out in situ where SPION were prepared in the presence of the *f*-MWNTs. Iron (II) acetate was employed as the iron precursor for the formation of the SPION since it is water soluble and can be decomposed by thermal annealing. Samples with increasing amount of iron contents were prepared and the loading of SPION onto the MWNTs was subsequently determined. Iron (II) acetate (10, 20, 40, and 50 mg) was added to a round-bottomed flask containing 25 mg of functionalized MWNTs and 15 mL of distilled water. The mixture was bath sonicated for 10 min and stirred at 60 °C for 16 h to allow a uniform coverage of iron (II) acetate onto the surface the MWNTs. Solutions were left to cool down and filtered through a 0.2 µm polycarbonate membrane. Samples were then treated with $Ar/H_2$ at 500 °C for 2 h and left exposed in air thus affording the formation of the SPION on MWNTs surface.

*Analysis and Characterisation of SPION–MWNTs*: Thermogravimetric analyses were performed under flowing air at a heating rate of 10 °C/min up to 950 °C (Jupiter, Netzsch Instrument, Germany). X-ray diffraction studies were conducted using a powder diffractometer ($CuK_{\alpha 1}$, $\lambda$ = 0.1540 nm; Siemens D5000, Germany) with 2$\theta$ ranging from 5° to 65°. The PDF (powder data file) database was used to identify the compounds. For transmission electron microscopy studies, samples were prepared by dispersing a small amount of powder in absolute ethanol and sonicated using an ultrasonic power bath. The dispersions were placed dropwise onto lacey carbon grids. Low magnification TEM images were obtained using a JEOL 1210 transmission electron microscope (JEOL SAS, Japan) operating at 120 kV and high resolution TEM analysis was performed in an FEI Tecnai G2 microscope operating at 200 kV (Titan, FEI, the Netherlands). X-ray photoelectron spectra (XPS) were acquired with a Kratos AXIS ultra DLD. The magnetic moment of the samples was measured using a superconducting quantum interference device (SQUID, LOT-QuantumDesign Iberia, Spain) magnetometer. Each sample was placed into a diamagnetic gelatine capsule. Data was acquired with an applied field from –50 000 Oe to 50 000 Oe at temperatures of 10 K and 300 K. The sample holder contribution was subtracted in all the measurements.

*Preparation of SPION–MWNT Hybrids Dispersions for MR Studies*: SPION–MWNT hybrids dispersed in 1% Pluronic F127 solution were mixed with an equal volume of agar solution (2%, w/v in water) at 95 °C. Samples dispersions prepared at a range of Fe concentrations up to 1.25 mM were transferred to 0.3 mL microtubes within less than one minute before gel solidification occurs. Phantoms were imaged by MRI as described below.

*MR Imaging*: Phantom and in vivo MR imaging were performed at a 7T horizontal MR scanner (Agilent, Palo Alto, CA). The gradient coil had an inner diameter of 12 cm, gradient strength was 1000 mT/m (100 G/cm) and rise-time of 120 µs. A quadrature transmit/receive coil (RAPID Biomedical GmbH, Germany) with an internal diameter of 39 mm was used. Animals were intravenously injected with 0.72–4.4 mg Fe/kg S-MWNT 3 and imaged at 48 h post injection. This range of injection doses was chosen as reported in several pre-clinical studies.[19,28] Animals were imaged in prone position under constant anesthesia of 1.5% isoflurane/98.5% oxygen. Body temperature was maintained constant at 37 °C using a warm air fan and ECG and respiration monitored (SA Instruments, Stony Brook, NY). $R_2$* imaging was used in this study as it does not only reflect the spin-spin relaxation but also takes into account the magnetic field inhomogeneity. Cine-FLASH MRI technique with variable echo time (TE) was used to acquire $R_2$* images and such methods were adopted both in vitro and in vivo. The cine-FLASH parameters for $R_2$* images in phantoms were: FOV = 30 × 30 mm, matrix size = 96 × 96, slice thickness = 1 mm; number of slice = 1; flip angle = 20°, 1 average, TR = 700 ms; TE = 1, 2, 3, 5, 8, 10 ms; scan time ~ 7 min. Cine-FLASH parameters for in vivo $R_2$* acquisitions were: FOV = 25 × 25 mm, matrix size = 128 × 128, slice thickness = 1 mm; flip angle = 20°; number of slice = 1; 1 average; TR = 1/heart rate = RR-interval; TE = 1, 2, 3, 5 ms; scan time ~10 min. A short-axis and a long axis view were used for the in-vivo experiment.

*MR Image Analysis*: MR images were analyzed using the ImageJ software (NIH, USA). $R_2$* pixel by pixel data was fitted by the following equation:

$$S_n = S_0 * EXP(-TE_n / T_2^*) \quad (1)$$

where $S_n$ is the signal measured, $S_0$ is the initial signal and $TE_n$ represents the different echo spacing. By selecting a region of interest (ROI) within the phantom area or, for in vivo studies, within the liver area, the software automatically calculates mean $T_2$* values. $R_2$* values ($1/T_2$*) were plotted using Excel versus the corresponding iron concentrations. Results are presented as mean ± S.D. (n = 3). In phantom studies such plot resulted in a linear relationship where the slopes corresponded to the $r_2$*relaxivities.

*Radio-Labelling of S-MWNT Hybrid* 1–3: The labelling of SPION-MWNT hybrids with $^{99m}$Tc-BP was carried out as previously reported by de Rosales et al.[26,28] Hybrids with different iron contents were tested initially to optimise the radio-labelling efficiency. S-MWNT 1–3 (125 µg/125 µL) were first dispersed by sonication (10 min) in 1% Pluronic F127 solution at 1 mg/mL concentration and mixed with 1–10 MBq $^{99m}$Tc-BP (500 MBq in 50 µg of BP/125 µL). The mixture was incubated at 37 °C for 30 min with gentle shaking. After cooling to room temperature, $^{99m}$Tc-BP-S-MWNT hybrids were separated from unbound $^{99m}$Tc-BP by centrifugation at 17 000 rcf for 10 min and the pellets containing $^{99m}$Tc-BP-S-MWNT hybrids were washed 4 times (1 mL each wash) with 1% Pluronic F127 until no radioactivity was detected in the supernatant. The total radioactivity in the supernatants and the pellet were measured to determine the radio-labelling efficiency. The pellet was then re-dispersed using 1% Pluronic F127 solution to achieve a final concentration of 1 mg/mL for subsequent in vivo studies ($\gamma$-scintigraphy and SPECT/CT imaging).

*In Vitro Stability in PBS and Human Serum*: To assess the in vitro stability of the radio-labelled hybrids, $^{99m}$Tc-BP-S-MWNT 1–3 were mixed with an equal volume of human serum or PBS (at 50% final concentration) and incubated at 37 °C under constant shaking for 24 h. The samples were then centrifuged at 17 000 rcf for 10 min. The radioactivity of the pellets and the supernatants were measured by gamma counting to determine the percentage of $^{99m}$Tc-BP remained bound to the S-MWNT hybrids representing stably labelled hybrids.

*Whole Body 3D SPECT/CT Imaging of Mice Injected with $^{99m}$Tc-BP-S-MWNT* 3: All in vivo experiments were conducted under the authority of project and personal licences granted by the UK Home Office and the UKCCCR Guidelines (1998). C57/Bl6 mice were anaesthetised by isofluorane inhalation and injected intravenously with 50 µg of $^{99m}$Tc-BP-S-MWNT 3 or $^{99m}$Tc-BP in 1% Pluronic F127 solution containing approximately 5 MBq. SPECT imaging was carried out immediately after injection with images taken in 16 projections over 30 min using a four-head scanner with 1.4 mm pinhole collimators (Nano-SPECT/CT scanner, Bioscan, USA). CT scanning was performed with a 45 kV X-ray source and 1000 ms exposure time over 10 min at the end of each SPECT acquisition. SPECT and CT images were reconstructed using the MEDISO software (Medical Imaging Systems) and then merged by the InVivoScope software (Bioscan, USA). Each animal was recovered and further imaged at 4 h and 24 h.

*Organ Biodistribution of $^{99m}$Tc-BP-S-MWNT* 3 *in Mice by Gamma Scintigraphy*: The pharmacokinetic studies including the blood circulation and organ biodistribution of the hybrid were carried out using female C57/Bl6 mice (6–8 weeks old). Mice were given 50 µg of $^{99m}$Tc-BP-S-MWNT 3 or $^{99m}$Tc-BP (250 µL in 1% Pluronic F127 solution) intravenously *via* tail vein. The blood clearance profile was established by collecting blood samples in heparinised capillaries from 2 min up to 24 h after injection. For organ biodistribution study, major organs including skin, liver, spleen, heart, lung, muscle, bone, brain, stomach, and intestine were excised post mortem at 1 h, 4 h, and 24 h after injection. Samples were weighed and the radioactivity was detected, quantified and corrected for physical radioisotope decay by gamma scintigraphy. The % ID per organ and per gram tissue were calculated and plotted as the mean of triplicate or quadruplicate samples ± SD.

*Histological Analysis*: For histological examination of organs, C57/Bl6 mice were injected via tail vein with 400 µg of S-MWNT 3 (5.8 mg Fe/kg) dispersed in 1% Pluronic F127 solution and tissues of lung, liver, and spleen were excised at 24 h, 7 days, and 30 days after injection. Lung tissues were sampled by an inflation-fixation method. Mice were given an overdose of pentobarbital sodium intraperitonealy and a small incision in the midline of the trachea was performed. A 24 gauge catheter (Angiocath, BD Biosciences, UK) was placed in the mouse trachea and a solution of 5 mL 10% neutral buffered formalin (Sigma-Aldrich, UK) was directly instilled into the lung using a syringe. Entire inflated lung was removed and stored in 10% neutral buffer formalin. Other organs were immediately fixed in 10% neutral buffer formalin as 5 mm$^2$ pieces. Samples were then wax-embedded and sectioned for haematoxylin and eosin stains (H&E) or Neutral Red stains according to standard histological protocols at the Royal Veterinary College.

To detect the presence of iron in tissues, Perls staining was carried out using a Perls stain kit used according to the manufacturer's instruction. In brief, sections were deparaffinised and incubated with potassium ferrocyanide solution for 20 min followed by counterstaining with nuclear red solution for 10 min. Sections were then dehydrated using increasing concentrations of ethanol solutions (70%, 90%, and absolute ethanol), cleared by xylene and mounted in DPX.

All stained sections were analysed using a Leica DM 1000 LED Microscope (Leica Microsystems, UK) coupled with CDD digital camera (Qimaging, UK).

*TEM Examination of S-MWNT* 3 *in Liver and Spleen Tissues*: Mice were injected with 400 µg of S-MWNT 3 (5.8 mg Fe/kg) dispersed in 1% Pluronic F127 solution. At 24 h, mice were killed and liver and spleen were rinsed by PBS. Organs were excised into 2 mm thin pieces and fixed in 2.5% EM grade glutaldehyde in 0.1 M sodium cacodylate buffer for 24 h. Liver and spleen samples were then transferred to 0.1 M sodium cacodylate buffer and stored at 4 °C until further processing. Samples were fixed using 1% osmium oxide solution for 3 h. The samples were rinsed with 0.1 M cacodylate buffer and de-hydrated using increasing concentrations of ethanol solutions (70%, 90%, and absolute ethanol). Propylene oxide was added to the samples for 15 min, followed by infiltration in 1:1 mixture of propylene oxide: epoxy resin (Araldite CY212, DDSA and DMP30) overnight. The samples were then embedded into epoxy resin blocks and left in 60 °C oven for 3 days to polymerise. Ultrathin sections were cut on a microtome (Leica Reichert Ultracut) using a diamond knife and collected on 300-mesh copper grids. The grids were stained using uranyl acetate and imaged using a FEI/Philips CM12 transmission electron microscope (FEI, the Netherlands) at 80 kV.

## Supporting Information

Supporting Information is available from the Wiley Online Library or from the author.

## Acknowledgements

J. T.-W. Wang and L. Cabana contributed equally to this work. Funding from Biotechnology and Biological Sciences Research Council (BB/J008656/1), Associated International Cancer Research, Spanish Ministerio de Economía y Competitividad (MAT2011-24757), the EU FP7-ITN Marie-Curie Network programme RADDEL (290023), and the EU FP7-Integrated Infrastructure Initiative–I3 programme ESTEEM2 (312483) is acknowledged. H. Kafa is supported by the Atomic Energy Commission of Syria. L. Cabana is supported by a CSIC JAE Predoc Fellowship and is enrolled in the UAB PhD program. R. T. M. de Rosales acknowledges funding by The Centre of Excellence in Medical Engineering funded by the Wellcome Trust and EPSRC under Grant No. WT 088641/Z/09/Z. X. Ke and G. Van Tendeloo acknowledge funding from the European Research Council under the Seventh Framework Program (FP7) ERC Grant No 246791- COUNTATOMS. K. T. Al-Jamal, G. Tobias and R. T. M. de Rosales thank the members of the EU COST actions TD1004 (Theranostics Imaging and Therapy: An Action to Develop Novel Nanosized Systems for Imaging-Guided Drug Delivery) and TD1007 (Bimodal PET-MRI molecular imaging technologies and applications for in vivo monitoring of disease and biological processes) for useful discussions.

Received: August 17, 2013
Revised: October 4, 2013
Published online: November 19, 2013

[1] J. Cheon, J. H. Lee, *Acc. Chem. Res.* **2008**, *41*, 1630.
[2] J. V. Jokerst, S. S. Gambhir, *Acc. Chem. Res.* **2011**, *44*, 1050.
[3] X. Michalet, F. F. Pinaud, L. A. Bentolila, J. M. Tsay, S. Doose, J. J. Li, G. Sundaresan, A. M. Wu, S. S. Gambhir, S. Weiss, *Science* **2005**, *307*, 538.
[4] S. K. Nune, P. Gunda, P. K. Thallapally, Y. Y. Lin, M. L. Forrest, C. J. Berkland, *Expert Op. Drug Deliv.* **2009**, *6*, 1175.
[5] A. Bianco, K. Kostarelos, C. D. Partidos, M. Prato, *Chem. Commun.* **2005**, 571.
[6] K. T. Al-Jamal, F. M. Toma, A. Yilmazer, H. Ali-Boucetta, A. Nunes, M. A. Herrero, B. W. Tian, A. Eddaoui, W. T. Al-Jamal, A. Bianco, M. Prato, K. Kostarelos, *FASEB J.* **2010**, *24*, 4354.
[7] Z. Liu, S. Tabakman, K. Welsher, H. J. Dai, *Nano Res.* **2009**, *2*, 85.
[8] S. Keren, C. Zavaleta, Z. Cheng, A. De La Zerda, O. Gheysens, S. S. Gambhir, *Proc. Natl. Acad. Sci. USA* **2008**, *105*, 5844.
[9] N. W. S. Kam, M. O'Connell, J. A. Wisdom, H. J. Dai, *Proc. Natl. Acad. Sci. USA* **2005**, *102*, 11600.

[10] A. De La Zerda, C. Zavaleta, S. Keren, S. Vaithilingam, S. Bodapati, Z. Liu, J. Levi, B. R. Smith, T. J. Ma, O. Oralkan, Z. Cheng, X. Y. Chen, H. J. Dai, B. T. Khuri-Yakub, S. S. Gambhir, *Nature Nanotechnol.* **2008**, *3*, 557.
[11] L. G. Delogu, G. Vidili, E. Venturelli, C. Ménard-Moyon, M. A. Zoroddu, G. Pilo, P. Nicolussi, C. Ligios, D. Bedognetti, F. Sgarrella, R. Manetti, A. Bianco, *Proc. Natl. Acad. Sci. USA* **2012**, *109*, 16612.
[12] C. Balas, *Meas. Sci. Technol.* **2009**, *20*, 104020.
[13] D. McRobbie, E. Moore, M. Graves, M. Prince, *MRI from Picture to Proton*, Cambridge University Press, UK **2006**.
[14] A. B. de Barros, A. Tsourkas, B. Saboury, V. N. Cardoso, A. Alavi, *EJNMMI Res.* **2012**, *2*, 39.
[15] A. Louie, *Chem. Rev.* **2010**, *110*, 3146.
[16] B. Sitharaman, K. R. Kissell, K. B. Hartman, L. A. Tran, A. Baikalov, I. Rusakova, Y. Sun, H. A. Khant, S. J. Ludtke, W. Chiu, S. Laus, E. Toth, L. Helm, A. E. Merbach, L. J. Wilson, *Chem. Commun.* **2005**, 3915.
[17] B. Sitharaman, B. D. Jacobson, Y. Z. Wadghiri, H. Bryant, J. Frank, *J. Appl. Phys.* **2013**, *113*, 134308.
[18] J. H. Choi, F. T. Nguyen, P. W. Barone, D. A. Heller, A. E. Moll, D. Patel, S. A. Boppart, M. S. Strano, *Nano Lett.* **2007**, *7*, 861.
[19] H. X. Wu, G. Liu, Y. M. Zhuang, D. M. Wu, H. Q. Zhang, H. Yang, H. Hu, S. P. Yang, *Biomaterials* **2011**, *32*, 4867.
[20] B. Chen, H. Zhang, C. Zhai, N. Du, C. Sun, J. Xue, D. Yang, H. Huang, B. Zhang, Q. Xie, Y. Wu, *J. Mater. Chem.* **2010**, *20*, 9895.
[21] B. T. Doan, J. Seguin, M. Breton, R. Le Beherec, M. Bessodes, J. A. Rodriguez-Manzo, F. Banhart, J. C. Beloeil, D. Scherman, C. Richard, *Contrast Media Mol. I.* **2012**, *7*, 153.
[22] M. Yin, M. L. Wang, F. Miao, Y. X. Ji, Z. Tian, H. B. Shen, N. Q. Jia, *Carbon* **2012**, *50*, 2162.
[23] A. Li, C. S. Wong, M. K. Wong, C. M. Lee, M. C. A. Yeung, *Br. J. Radiol.* **2006**, *79*, 368.
[24] A. J. Gauden, P. M. Phal, K. J. Drummond, *J. Clin. Neurosci.* **2010**, *17*, 1097.
[25] Y. X. Wang, *Quant. Imaging Med. Surg.* **2011**, *1*, 35.
[26] L. Lartigue, D. Alloyeau, J. Kolosnjaj-Tabi, Y. Javed, P. Guardia, A. Riedinger, C. Péchoux, T. Pellegrino, C. Wilhelm, F. Gazeaut, *ACS Nano* **2013**, *7*, 3939.
[27] S. W. A. Bligh, P. J. Sadler, J. A. Marriott, I. A. Latham, J. D. Kelly, *Appl. Radiat. Isot.* **1989**, *40*, 751.
[28] J. S. Choi, J. C. Park, H. Nah, S. Woo, J. Oh, K. M. Kim, G. J. Cheon, Y. Chang, J. Yoo, J. Cheon, *Angew. Chem. Int. Ed. Engl.* **2008**, *47*, 6259.
[29] C. Glaus, R. Rossin, M. J. Welch, G. Bao, *Bioconjug. Chem.* **2010**, *21*, 715.
[30] B. R. Jarrett, B. Gustafsson, D. L. Kukis, A. Y. Louie, *Bioconjug. Chem.* **2008**, *19*, 1496.
[31] N. Kohler, C. Sun, A. Fichtenholtz, J. Gunn, C. Fang, M. Q. Zhang, *Small* **2006**, *2*, 785.
[32] J. R. McCarthy, R. Weissleder, *Adv. Drug Deliv. Rev.* **2008**, *60*, 1241.
[33] L. Sandiford, A. Phinikaridou, A. Protti, L. K. Meszaros, X. J. Cui, Y. Yan, G. Frodsham, P. A. Williamson, N. Gaddum, R. M. Botnar, P. J. Blower, M. A. Green, R. T. M. de Rosales, *ACS Nano* **2013**, *7*, 500.
[34] R. Torres Martin de Rosales, C. Finucane, S. J. Mather, P. J. Blower, *Chem. Commun.* **2009**, 4847.
[35] R. Torres Martin de Rosales, R. Tavare, A. Glaria, G. Varma, A. Protti, P. J. Blower, *Bioconjug. Chem.* **2011**, *22*, 455.
[36] R. Torres Martin de Rosales, R. Tavare, R. L. Paul, M. Jauregui-Osoro, A. Protti, A. Glaria, G. Varma, I. Szanda, P. J. Blower, *Angew. Chem. Int. Ed. Engl.* **2011**, *50*, 5509.
[37] G. Tobias, L. D. Shao, C. G. Salzmann, Y. Huh, M. L. H. Green, *J. Phys. Chem. B* **2006**, *110*, 22318.
[38] L. Shao, G. Tobias, C. G. Salzmann, B. Ballesteros, S. Y. Hong, A. Crossley, B. G. Davis, M. L. H. Green, *Chem. Commun.* **2007**, 5090.
[39] J. Liu, A. G. Rinzler, H. J. Dai, J. H. Hafner, R. K. Bradley, P. J. Boul, A. Lu, T. Iverson, K. Shelimov, C. B. Huffman, F. Rodriguez-Macias, Y. S. Shon, T. R. Lee, D. T. Colbert, R. E. Smalley, *Science* **1998**, *280*, 1253.
[40] B. Ballesteros, G. Tobias, L. Shao, E. Pellicer, J. Nogues, E. Mendoza, M. L. H. Green, *Small* **2008**, *4*, 1501.
[41] R. M. Lago, S. C. Tsang, K. L. Lu, Y. K. Chen, M. L. H. Green, *J. Chem. Soc. Chem. Comm.* **1995**, *0*, 1355.
[42] T. Kolodiazhnyi, M. Pumera, *Small* **2008**, *4*, 1476.
[43] A. Ambrosi, M. Pumera, *Chemistry* **2010**, *16*, 10946.
[44] A. P. Grosvenor, B. A. Kobe, M. C. Biesinger, N. S. McIntyre, *Surf. Interface Anal.* **2004**, *36*, 1564.
[45] K. T. Al-Jamal, A. Nunes, L. Methven, H. Ali-Boucetta, S. Li, F. M. Toma, M. A. Herrero, W. T. Al-Jamal, H. M. M. ten Eikelder, J. Foster, S. Mather, M. Prato, A. Bianco, K. Kostarelos, *Angew. Chem. Int. Ed.* **2012**, *51*, 6389.
[46] S. Y. Hong, G. Tobias, K. T. Al-Jamal, B. Ballesteros, H. Ali-Boucetta, S. Lozano-Perez, P. D. Nellist, R. B. Sim, C. Finucane, S. J. Mather, M. L. Green, K. Kostarelos, B. G. Davis, *Nat. Mater.* **2010**, *9*, 485.
[47] B. J. Pichler, A. Kolb, T. N gele, H. P. Schlemmer, *J. Nucl. Med.* **2010**, *51*, 333.
[48] G. Lamanna, A. Garofalo, G. Popa, C. Wilhelm, S. Begin-Colin, D. Felder-Flesch, A. Bianco, F. Gazeau, C. Ménard-Moyon, *Nanoscale* **2013**, *5*, 4412.
[49] B. Ballesteros, G. Tobias, M. A. H. Ward, M. L. H. Green, *J. Phys. Chem. C* **2009**, *113*, 2653.
[50] R. M. Cornell, U. Schwertmann, *The Iron Oxides: Structure, Properties, Reactions, Occurrence and Uses* USA: John Wiley & Sons, Ltd., **1996**.
[51] X. Batlle, A. Labarta, *J. Phys. D—Appl. Phys.* **2002**, *35*, R15.
[52] C. W. Jung, P. Jacobs, *Magn. Reson. Imaging* **1995**, *13*, 661.
[53] M. Rohrer, H. Bauer, J. Mintorovitch, M. Requardt, H. J. Weinmann, *Invest. Radiol.* **2005**, *40*, 715.
[54] R. Misri, D. Meier, A. Yung, P. Kozlowski, U. Haumlfeli, *Nanomed. Nanotechnol. Biol. Med.* **2012**, *8*, 1007.
[55] C. Chambon, O. Clement, A. Leblanche, E. Schoumanclaeys, G. Frija, *Magn. Reson. Imaging* **1993**, *11*, 509.
[56] P. Reimer, B. Tombach, *Eur. Radiol.* **1998**, *8*, 1198.
[57] K. Donaldson, F. A. Murphy, R. Duffin, C. A. Poland, *Part. Fibre Toxicol.* **2010**, *7*, 5.
[58] L. Lacerda, H. Ali-Boucetta, M. A. Herrero, G. Pastorin, A. Bianco, M. Prato, K. Kostarelos, *Nanomedicine* **2008**, *3*, 149.
[59] L. Lacerda, A. Soundararajan, R. Singh, G. Pastorin, K. T. Al-Jamal, J. Turton, P. Frederik, M. A. Herrero, S. L. A. Bao, D. Emfietzoglou, S. Mather, W. T. Phillips, M. Prato, A. Bianco, B. Goins, K. Kostarelos, *Adv. Mater.* **2008**, *20*, 225.
[60] V. Kubíček, J. Rudovský, J. Kotek, P. Hermann, L. Vander Elst, R. N. Muller, Z. I. Kolar, H. T. Wolterbeek, J. A. Peters, I. Lukeš, *J. Am. Chem. Soc.* **2005**, *127*, 16477.